

Article

Improving Anti-Coking Properties of Ni/Al₂O₃ Catalysts via Synergistic Effect of Metallic Nickel and Nickel Phosphides in Dry Methane Reforming

Yu Shi, Shiwei Wang, Yiming Li, Fan Yang, Hongbo Yu, Yuting Chu, Tong Li *  and Hongfeng Yin *

Ningbo Institute of Materials Technology and Engineering, Chinese Academy of Sciences, 1219 Zhongguan West Road, Ningbo 315201, China; shiyu@nimte.ac.cn (Y.S.); wangshiwei@nimte.ac.cn (S.W.); liyiming@nimte.ac.cn (Y.L.); yf@nimte.ac.cn (F.Y.); yuhongbo@nimte.ac.cn (H.Y.); chuyuting@nimte.ac.cn (Y.C.)
* Correspondence: litong@nimte.ac.cn (T.L.); yinhf@nimte.ac.cn (H.Y.)

Abstract: A series of NiP-x/Al₂O₃ catalysts containing different ratio of metallic nickel to nickel phosphides, prepared by varying Ni/P molar ratio of 4, 3, 2 through a co-impregnation method, were employed to investigate the synergistic effect of metallic nickel-nickel phosphides in dry methane reforming reaction. The Ni/Al₂O₃ catalyst indicates good activity along with severe carbon deposition. The presence of phosphorus increases nickel dispersion as well as the interaction between nickel and alumina support, which results in smaller nickel particles. The co-existence of metallic nickel and nickel phosphides species is confirmed at all the P contained catalysts. Due to the relative stronger CO₂ dissociation ability, the NiP-x/Al₂O₃ catalysts indicate obvious higher resistance of carbon deposition. Furthermore, because of good balance between CH₄ dissociation and CO₂ dissociation, NiP-2/Al₂O₃ catalyst exhibits best resistance of carbon deposition, few carbon depositions were formed after 50 h of dry methane reforming.

Keywords: dry methane reforming; nickel catalysts; phosphides; coke-resistance; synergistic effect



Citation: Shi, Y.; Wang, S.; Li, Y.; Yang, F.; Yu, H.; Chu, Y.; Li, T.; Yin, H. Improving Anti-Coking Properties of Ni/Al₂O₃ Catalysts via Synergistic Effect of Metallic Nickel and Nickel Phosphides in Dry Methane Reforming. *Materials* **2022**, *15*, 3044. <https://doi.org/10.3390/ma15093044>

Academic Editor: Lucjan Chmielarz

Received: 31 March 2022

Accepted: 19 April 2022

Published: 22 April 2022

Publisher's Note: MDPI stays neutral with regard to jurisdictional claims in published maps and institutional affiliations.



Copyright: © 2022 by the authors. Licensee MDPI, Basel, Switzerland. This article is an open access article distributed under the terms and conditions of the Creative Commons Attribution (CC BY) license (<https://creativecommons.org/licenses/by/4.0/>).

1. Introduction

Dry reforming of methane, described as $\text{CH}_4 + \text{CO}_2 = 2\text{H}_2 + 2\text{CO}$, has been intensively studied since it was reported [1]. It has two obvious advantages: the reactants of dry methane reforming are two kinds of greenhouse gases (CH₄ and CO₂). On the other hand, the low H₂/CO ratio for the products of dry methane reforming (DMR) is suitable for the Fischer–Tropsch synthesis and methanol synthesis [2,3].

Catalysts play crucial roles during dry methane reforming process. Noble metals, such as Ru, Rh, Pd, Pt, and Ir, display excellent catalytic performance and good stability in dry methane reforming, whereas the limits of resources and high costs restrict their utilization scales on the industry. Transition metals, such as Fe, Cu, Co, especially Ni, have been proved a kind of efficient catalysts for dry methane reforming [4,5]. However, due to the relative stronger methane dissociation ability of transition metals, the carbon deposition over transition metals is a crucial problem which is the restriction for the utilization [6].

As is shown in the literatures [7], carbon deposition on the surface of nickel catalyst is generally carried out according to the following steps: methane molecules dissociate on the metal surface to generate adsorbed CH_x-* species, which will be further dehydrogenated to form C-*; part of the C-* species can be removed by the surface active O-* species generated from the dissociation of CO₂ molecules and convert into CO; at the same time, the unconverted CH_x-* will further undergo deep cracking on the metal surface to form surface carbon; In addition, the further aggregation of adsorbed CH_x-* species is another way to form carbon deposits. It follows that increasing the adsorption and dissociation rate of CO₂ and appropriately reducing the methane dissociation ability of the catalyst are effective ways to inhibit the carbon deposition on the surface of nickel catalyst.

Many endeavors have been studied to suppress the carbon deposition over nickel catalyst in dry methane reforming. These studies mainly focus on: (1) Enhance the surface basicity of the catalysts by the addition of alkaline promoters, which increases the CO₂ dissociation ability, promotes the generation of surface-active O^{-*} species and enhances the elimination of surface C^{-*} species on nickel catalysts. The promotion of alkalis [8], alkaline-earth metals [9,10], and rare-earth metals (La, Ce) [11,12] can enhance the dispersion of nickel species and the surface basicity and promote the generation of surface active O^{-*} species from CO₂, which results in better carbon deposition resistance over nickel catalysts, whereas the enhancement of surface basicity always accompanies the decrease of methane dissociation rate, which leads to the decrease of activity [8]. (2) Obtain smaller nickel nanoparticle size by confining nickel species with mesoporous materials [13,14], inorganic shells [11,15], and the edge of the support [3], which is beneficial of the resistance for carbon formation during DMR. Wang et al. [13] investigated S-2 zeolite fixed nickel nanoparticles structure catalyst (Ni@S-2) in DMR and found Ni@S-2 exhibited superb carbon resistance. Liu et al. [16] synthesized a multiple-core@shell structured catalyst (Ni-ZrO₂@SiO₂) catalyst and investigated its catalytic performance in DMR. Due to the small nickel nanoparticle size and the confinement effect of SiO₂ shell, Ni-ZrO₂@SiO₂ displayed ultra-high coking resistance for dry methane reforming. Song et al. [3] found that the edges of MgO crystals exhibited good properties of the stabilization of nickel nanoparticles, which resulted in good resistance of carbon deposition in DMR. What is more, special structure catalysts, such as spinels (NiAl₂O₄ [17], Ni/MgAl₂O₄ [18]), perovskites (LaNiO₃ [19], La_{1-x}Pr_xNiO_{3-δ} [20], La_{0.6}Sr_{0.2}Ti_{0.85}Ni_{0.15}O_{3-δ} [21]), hydrotalcites (Ce-NiMgAl hydrotalcite [22], Zr-NiMgAl hydrotalcite [23], La-NiMgAl hydrotalcite [24]), and solid solutions (NiOMgO [25], NiO-CeO₂ [26]), which have a strong ability for confining nickel nanoparticles, are also used to increase the carbon resistance of nickel catalysts; (3) Decrease the outer electron cloud density of nickel catalyst by alloying nickel with other metals [27,28], which decreases CH₄ dissociation ability of the catalysts. Turap et al. [27] indicated that Co-Ni alloy promoted the adsorption of surface oxygen and enhanced carbon removal, resulting in less carbon deposition compared to nickel catalyst; (4) Poison CH₄ dissociation ability of nickel with sulfur [29], which, however, passivates the activity of nickel catalysts in dry methane reforming.

Transition metal carbides, such as Mo₂C and WC, which have similar outer electronic structure to noble metals, are becoming an attractive and promising catalyst for replacement of traditional dry methane reforming catalysts due to their excellent resistance to carbon deposition [30–32]. However, due to the relative strong CO₂ dissociation properties, transition metal carbides are easy oxidized by CO₂ to inactive oxides phase, which leads to rapid deactivation during dry methane reforming process at atmospheric pressure. Subsequently, Ni–Mo₂C catalysts were found to show stable DMR activity at atmospheric pressure [32,33]. Ni species are proposed to be in charge of the dissociation of CH₄, while Mo₂C is responsible for the dissociation of CO₂. However, the appropriate molar ratio of Ni to carbides is controversial in different literatures. Shi et al. [33] reported that the optimum Ni/Mo₂C ratio was 1/2, while Cheng et al. [34] reported that the catalyst with Ni/Mo₂C = 1/10 exhibited best stability.

Recently, transition metal phosphides (MoP, WP, NiP_x) were demonstrated to exhibit better activity, stability, and higher resistance of oxidation and coking than Ni/Mo₂C catalyst in dry methane reforming [35,36]. However, transition metals phosphide catalysts still exhibit relative stronger CO₂ dissociation properties than CH₄ dissociation properties. Yao et al. [35] found that bulk MoP catalyst preferred low temperature and space velocity for DMR, the oxidation by CO₂ to MoO₂ species was also observed at the condition of relative high temperature and WHSV. González-Castaño et al. [37] investigated the catalytic performance of 20 wt% Ni₂P supported on Al₂O₃, CeO₂, and SiO₂-Al₂O₃, and the result indicated that the Ni₂P/Al₂O₃ catalyst showed highest conversion and stability. However, visible deactivation was still observed after 10 h of time on stream, which was due to the oxidation of Ni₂P phase during dry methane reforming. Further improvement of metal

phosphides catalysts in DMR is therefore highly desirable to develop a new catalyst which is resistant to coking for the atmospheric DMR reaction.

Considering that the combination of the strong ability for dissociating methane of metallic Ni and strong ability for cracking carbon dioxide of Mo_2C has exhibited excellent catalytic performance and anti-coking property, as a consequence, the system of metallic nickel and transition metal phosphide is worth taking into account for the DMR process. Herein, we developed a new metallic nickel–nickel phosphides catalyst system for DMR to cope with the inherent coking problem of Ni-based catalysts. Through incipient wetness impregnation method, we prepared a series of catalysts with different Ni/P molar ratio supported on the alumina. The catalysts were tested in DMR process at 700 °C and atmospheric pressure. At the same time, we attempted to clarify the effect of the addition of P on the catalyst properties and coke resistance in the DMR reaction.

2. Experimental

2.1. Catalyst Preparation

The Ni-based catalysts were prepared by an incipient wetness impregnation method with an aqueous solution of nickel nitrate hexahydrate ($\text{Ni}(\text{NO}_3)_2 \cdot 6\text{H}_2\text{O}$, AR, Sinopharm Chemical Reagent Co., Ltd., Shanghai, China). The impregnated samples were dried at 110 °C overnight, and then calcined at 800 °C in air for 4 h. P was introduced in the catalysts by co-impregnation method with diammonium hydrogen phosphate ($(\text{NH}_4)_2\text{HPO}_4$, AR, Shanghai Aladdin Biochemical Technology Co., Ltd., Shanghai, China) as a precursor. Citric acid (AR, Sinopharm Chemical Reagent Co., Ltd., Shanghai, China) was employed as complexing agent with the same mole of nickel to avoid the generation of Ni-PO_4 precipitation. Before dry methane reforming measurement, the catalysts were reduced at 900 °C for 2 h with pure H_2 flow. The loading content of Ni was fixed at 10 wt.% ($m_{\text{Ni}}/m_{\text{catalyst}}$), and P-free catalyst was denoted as $\text{Ni}/\text{Al}_2\text{O}_3$ while P-containing catalysts were denoted as $\text{NiP-x}/\text{Al}_2\text{O}_3$, where the x is the nominal atomic ratio of Ni:P.

2.2. Catalyst Characterization

Transmission electron microscopy (TEM) and high-resolution transition electron microscopy (HRTEM) images were collected on a JEM 2100 transmission electron microscope (JEOL Ltd., Tokyo, Japan) and Tecnai F20 transmission electron microscope (FEI Company, Hillsboro, OR, USA) operating at 200 kV, respectively. High-angle annular dark field (HAADF) images in the STEM mode of the reduced catalysts were taken on a Talos F200 \times transmission electron microscope (Thermo Fisher Scientific, Waltham, MA, USA). The powder samples were dispersed in ethanol by ultrasonic and deposited on a copper grid to dry before measurement. At least ten representative images were taken for each sample. In order to obtain statistically reliable information, the size of at least 400 particles was measured.

X-ray diffraction (XRD) analyses of the bulk and crystalline structures of the catalysts were performed using a D8 ADVANCE X-ray diffractometer (Bruker Corporation, Karlsruhe, Germany) with $\text{Cu K}\alpha$ radiation. The scanned diffraction peaks were in the 2θ range between 10 and 90° with a scan speed of $5.7^\circ \cdot \text{min}^{-1}$. The assignment of the various crystalline phases was based on the ICSD diffraction file cards.

X-ray photoelectron spectroscopy (XPS) analyses of the reduced catalysts were performed on an X-ray photoelectron spectrometer (AXIS SUPRA, Shimadzu Corporation, Kyoto, Japan). The binding energies (BE) of Ni 2p and P 2p core-levels were recorded. The binding energy of the C 1s peak at 284.8 eV was taken as charge correction standard.

Elemental analyses of the reduced catalysts were performed by inductively coupled plasma optical emission spectrometry (ICP-OES) on a SPECTRO ARCOS II instrument (SPECTRO company, Kleve, Germany) to determine the elemental content and actual Ni/P atomic ratio.

Nitrogen adsorption–desorption measurements of the reduced catalysts were carried out on an ASAP 2460 apparatus (Micromeritics company, USA). Before the measurements,

~0.2 g catalysts were degassed under a flow of N₂ at 200 °C for 12 h. Specific surface areas (SSA) were calculated based on the Brunauer–Emmett–Teller (BET) equation at P/P₀ values in the range of 0.05–0.25. Pore sizes were determined by the Barrett–Joyner–Halenda (BJH) method using desorption isotherms.

Thermogravimetric analyses (TG) were performed on Diamond TG/DTA equipment from 25 to 800 °C at a heating rate of 10 °C·min⁻¹ under air flow in order to quantify the carbon deposition formed on surface of the spent catalysts.

H₂ temperature programmed reduction (H₂-TPR) measurements of calcined catalysts were carried out with a VDSorb-91i apparatus (Quzhou Vodo Instrument Co., Ltd., Quzhou, China). The 0.05 g powder samples were pretreated at 200 °C for 30 min under N₂ flow at a rate of 30 mL·min⁻¹ and then cooled down to 50 °C. The samples were subsequently reduced by increasing the temperature to 1000 °C at a ramp rate of 10 °C·min⁻¹ in a stream of 8% H₂/Ar flow with a rate of 30 mL·min⁻¹. The H₂ consumption was determined with a thermal conductivity detector (TCD). A cooling trap placed between the sample and the detector retained the water formed during the reduction process.

Temperature programmed desorption of NH₃ (NH₃-TPD) analyses of the reduced catalysts were performed on an AutoChem II 2920 chemisorption apparatus (Micromeritics company, USA) in order to investigate the acidity of the catalysts. Prior to the analyses, ~0.05 g samples were pretreated at 300 °C for 60 min under He flow at rate of 30 mL·min⁻¹ and cooled down to 50 °C. Next, the samples were ammonia-saturated in a stream of 10% NH₃/He flow at rate of 30 mL·min⁻¹ for 60 min and then, the He was introduced for 30 min to remove the physical adsorbed NH₃. Finally, the samples were heated to 900 °C at a ramp rate of 10 °C·min⁻¹ under He flow.

In-situ CO₂ adsorption diffuse reflectance infrared Fourier transform spectroscopy (DRIFTS) analysis were recorded by a Thermo Nicolet 6700 infrared spectrometer (Thermo Fisher Scientific, Waltham, MA, USA) to obtain information about the plausible DMR reaction mechanism. The catalysts were initially reduced by H₂ and then purged with nitrogen at 300 °C for 30 min. After cooling down to 50 °C, 10 vol.% CO₂/N₂ mixture gas was introduced to the system. The spectral drift spectrum was recorded every 25 °C from 50–440 °C. Note that all spectra were recorded after 20 min exposure time when steady state conditions were reached.

2.3. Catalyst Performance Tests

The dry reforming of methane was carried out in a fixed-bed vertical quartz reactor (inner diameter = 8 mm) at atmospheric pressure. The reactor operated in a down flow mode and heated by a tubular resistance furnace. The bed of powder catalyst (100 mg, 20–40 mesh) was held in position by quartz wool and the thermocouple was placed near the catalyst bed tightly to measure the reaction temperature.

Before the DMR reaction tests, the catalysts were in-situ reduced at corresponding temperature at heating rate of 5 °C·min⁻¹ for 2 h under H₂ flow at a rate of 100 mL·min⁻¹. Later, the reaction temperature was ramped to 700 °C and maintained for different hours. The feed gas consisted of CH₄ (33.3 vol.%) and CO₂ (33.3 vol.%) diluted with N₂. Nitrogen was employed as the internal standard gas. The purity of the gases used in this work was 99.999 vol%. The outlet gas was analyzed using an online gas chromatograph (GC-7960 plus, Tengzhou Allen Analytical Instruments Co., Ltd., Tengzhou, China) equipped with a thermal conductivity detector and TDX-01 column.

3. Results and Discussion

3.1. Characterization of Fresh Catalysts

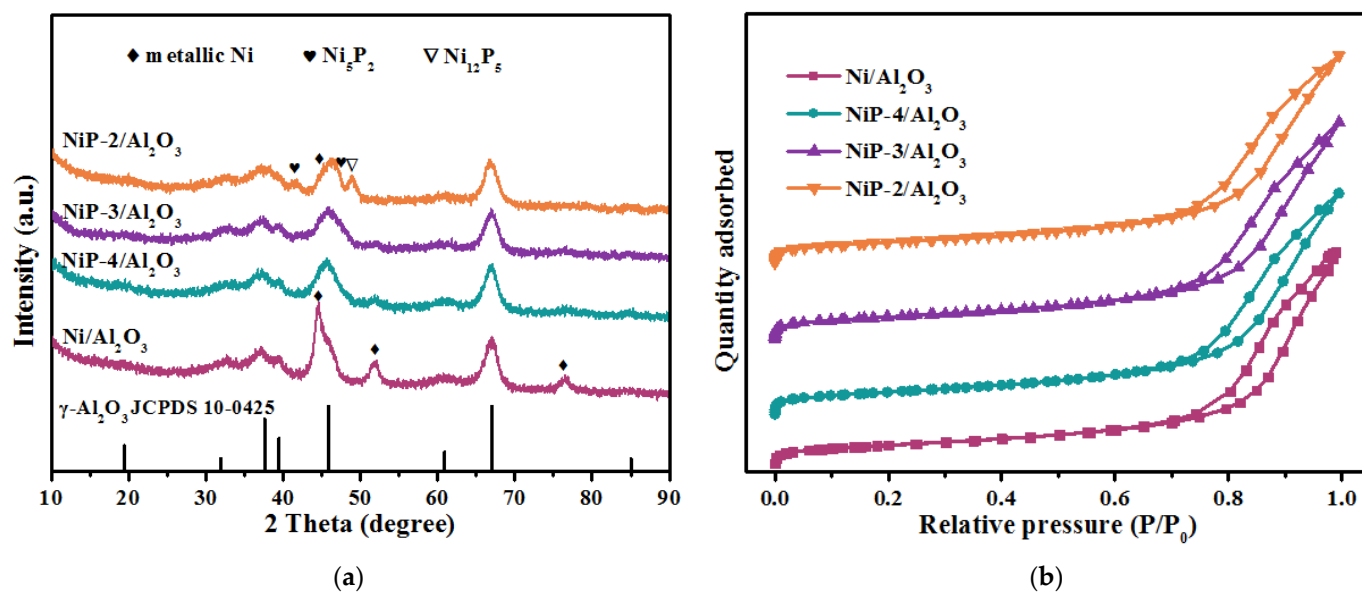
Element analysis of reduced catalysts, performed by ICP-OES, are displayed in Table 1. The measured contents of nickel and phosphorus roughly match with their nominal values, and the actual Ni/P molar ratios are basically in line with their expected values. This implies that there was no visible mass loss for phosphorus during reduction process at high temperature through PH₃ gas.

Table 1. Chemical composition, textural properties, and particle size distribution of reduced Al₂O₃ supported catalysts.

Catalyst	Chemical Composition			Textural Properties			Size ^b (nm)
	Ni ^a (wt.%)	P ^a (wt.%)	Ni/P Molar Ratio	S _{BET} (m ² /g)	V _{pore} (cm ³ /g)	D _{pore} (nm)	
Ni/Al ₂ O ₃	9.56	-	-	156	0.66	13.33	9.4 ± 2.1
NiP-4/Al ₂ O ₃	9.81	1.30	3.97	171	0.68	13.50	9.0 ± 1.6
NiP-3/Al ₂ O ₃	8.56	1.43	3.17	167	0.66	12.61	8.2 ± 1.5
NiP-2/Al ₂ O ₃	10.0	2.54	2.04	162	0.64	13.19	7.7 ± 1.6

^a Determined from ICP-OES. ^b Estimated by TEM.

The textural properties of the reduced catalysts, characterized by nitrogen adsorption–desorption measurements are summarized in Table 1 and the N₂ adsorption–desorption isotherms of Ni/Al₂O₃ and NiP-x/Al₂O₃ samples are shown in Figure 1b. Based on the IUPAC classification, the nitrogen isotherms can be classified as type IV, which is typical for mesoporous material [38]. With the change of P content, no significant change in the pore volume and average pore diameter of the catalysts was observed.

**Figure 1.** (a) XRD patterns and (b) N₂ adsorption–desorption isotherms of reduced Ni/Al₂O₃ and NiP-x/Al₂O₃ catalysts.

X-ray diffraction technology was used to study the crystal structure of reduced catalysts. The XRD patterns of reduced NiP-x/Al₂O₃ catalysts are presented in Figure 1a. Characteristic peaks at $2\theta = 31.94^\circ, 37.60^\circ, 39.49^\circ, 45.86^\circ, 67.03^\circ$ can be assigned to the crystalline phase of Al₂O₃ (JCPDS 10-0425) support. Characteristic peaks at 2θ of $44.49^\circ, 51.85^\circ, 76.38^\circ$ can be assigned to the crystallographic planes of metallic nickel phase (JCPDS 65-2865). Major peaks broadening indicates high dispersion of nickel phase on the alumina support. After the introduction of phosphorus, the further broadening of characteristic peaks of metallic nickel implies the better dispersion of nickel species. Besides, evident peak at 2θ of 48.96° along with broaden peaks at 2θ of $41.78^\circ, 47.65^\circ$, can be assigned to the crystallographic planes of Ni₁₂P₅ phase (JCPDS 22-1190) and Ni₅P₂ phase (JCPDS 17-0225), respectively, are observed over the NiP-2/Al₂O₃ catalyst, which implies the co-existence of metallic nickel and nickel phosphides. Due to the relative lower phosphorus content and partial peaks overlapping between Ni₁₂P₅, Ni₅P₂, and alumina, the characteristic peaks of nickel phosphides are hard to distinguish over NiP-4/Al₂O₃ and NiP-3/Al₂O₃ catalysts.

The morphologies of the samples are shown in Figure 2. For the P-containing catalysts, nanoparticles are evenly dispersed on the surface of Al_2O_3 (Figure 2b–d). The nickel particle size distributions of $\gamma\text{-Al}_2\text{O}_3$ supported catalysts are summarized in Table 1. Compared to $\text{Ni}/\text{Al}_2\text{O}_3$ (Figure S1), the $\text{NiP-x}/\text{Al}_2\text{O}_3$ show the smaller nickel particle size, which coincides with the XRD results. Furthermore, the EDS elemental mapping analyses indicate that the element distribution of P is always consistent with nickel species, which indicates that nickel species are prone to enrich at the phosphorus existence place (Figure 2j). Based on HRTEM images (Figure 2e–g), the lattice fringes spacing of individual particle is estimated for its identification. For all the reduced catalysts, the lattice fringes spacing of 0.201 nm, which corresponds well to the characteristic (1 0 1) plane of Ni species, is observed obviously on the nickel species nanoparticles. What is more, the lattice fringes spacing of 0.186 nm and 0.198 nm, ascribed to the (3 1 2) crystal plane of Ni_{12}P_5 and the (2 2 10) crystal plane of Ni_5P_2 , respectively, are observed at the reduced $\text{NiP-2}/\text{Al}_2\text{O}_3$ catalyst, (inset in Figure 2e–g). These results further confirm the co-existence of metallic nickel and nickel phosphides, which is in agreement with the results from the XRD of the reduced catalysts.

XPS analyses for the reduced catalysts were performed to investigate the surface valence states and electronic effects. Before the measurements, the catalysts have been passivated in order to be transferred from the quartz reactor to the XPS cell. The Ni 2p XPS spectrum of reduced catalysts is illustrated in Figure 3a. The broad enveloping peak of the Ni 2p signal can be deconvoluted in several separate overlapping doublets indicating that Ni exists in different chemical states:

- The peak at binding energy (BE) of 852.1–852.3 eV can be attributed to Ni^0 species which may be involved in metallic nickel [6,39].
- The peak at binding energy of 853.1–853.2 eV can be attributed to $\text{Ni}^{\delta+}$ ($0 < \delta < 2$) which may be involved in nickel phosphides species [40,41].
- The peak at binding energy of 855.3–856.5 eV can be attributed to Ni^{2+} which may be involved in Ni^{2+} in nickel phosphates or nickel aluminates species [39,42].

The presence of Ni^{2+} species can be explained by the passivation step which oxidized the surface Ni. However, it cannot be totally excluded that the presence of oxides can be due to incomplete reduction [43].

As shown in Figure 3a, Ni^0 and Ni^{2+} species along with their corresponding satellites are identified in the Ni 2p spectra of reduced $\text{Ni}/\text{Al}_2\text{O}_3$ samples. For the reduced P presence catalysts, the peaks at 853.1–853.2 eV, attributed to $\text{Ni}^{\delta+}$ species, are confirmed, which indicates the existence of nickel phosphides phase on the reduced $\text{NiP-x}/\text{Al}_2\text{O}_3$ catalysts. Table 2 displays the nickel species distribution obtained by XPS. The result indicates a considerable percentage of Ni^{2+} species (70.9%) and a low percentage of Ni^0 species (29.1%) on the $\text{Ni}/\text{Al}_2\text{O}_3$ catalyst. The percentage of $\text{Ni}^{\delta+}$ species increases with the increasing P content, which are obviously observed on the P presence catalysts. Moreover, the presence of P increases the percentage of Ni^0 and $\text{Ni}^{\delta+}$ while decreases Ni^{2+} species, which are observed on the reduced $\text{NiP-3}/\text{Al}_2\text{O}_3$ and $\text{NiP-2}/\text{Al}_2\text{O}_3$ catalysts. This may imply that the presence of P improves the reduction capacity of $\text{Ni}/\text{Al}_2\text{O}_3$ catalyst.

In P 2p spectra, as shown in Figure 3b, the broad enveloping peak of the P 2p signal can be deconvoluted in two separate overlapping doublets, indicating that P exists in different chemical states. The peak at binding energy of 129.8–129.9 eV can be assigned to $\text{P}^{\delta-}$ which may be involved in nickel phosphides species [40,41]; the peaks at binding energy of 133.5–133.7 eV can be attributed to P^{5+} and may be involved in phosphate species [35,41]. The presence of phosphates species may be due to the oxidation during passivation process and/or incomplete phase transformation during reduction process. The obvious peaks at 129.8–129.9 eV, attributed to $\text{Ni}^{\delta+}$ species, are confirmed on all the reduced $\text{NiP-x}/\text{Al}_2\text{O}_3$ catalysts, which strongly suggests the existence of nickel phosphides phase.

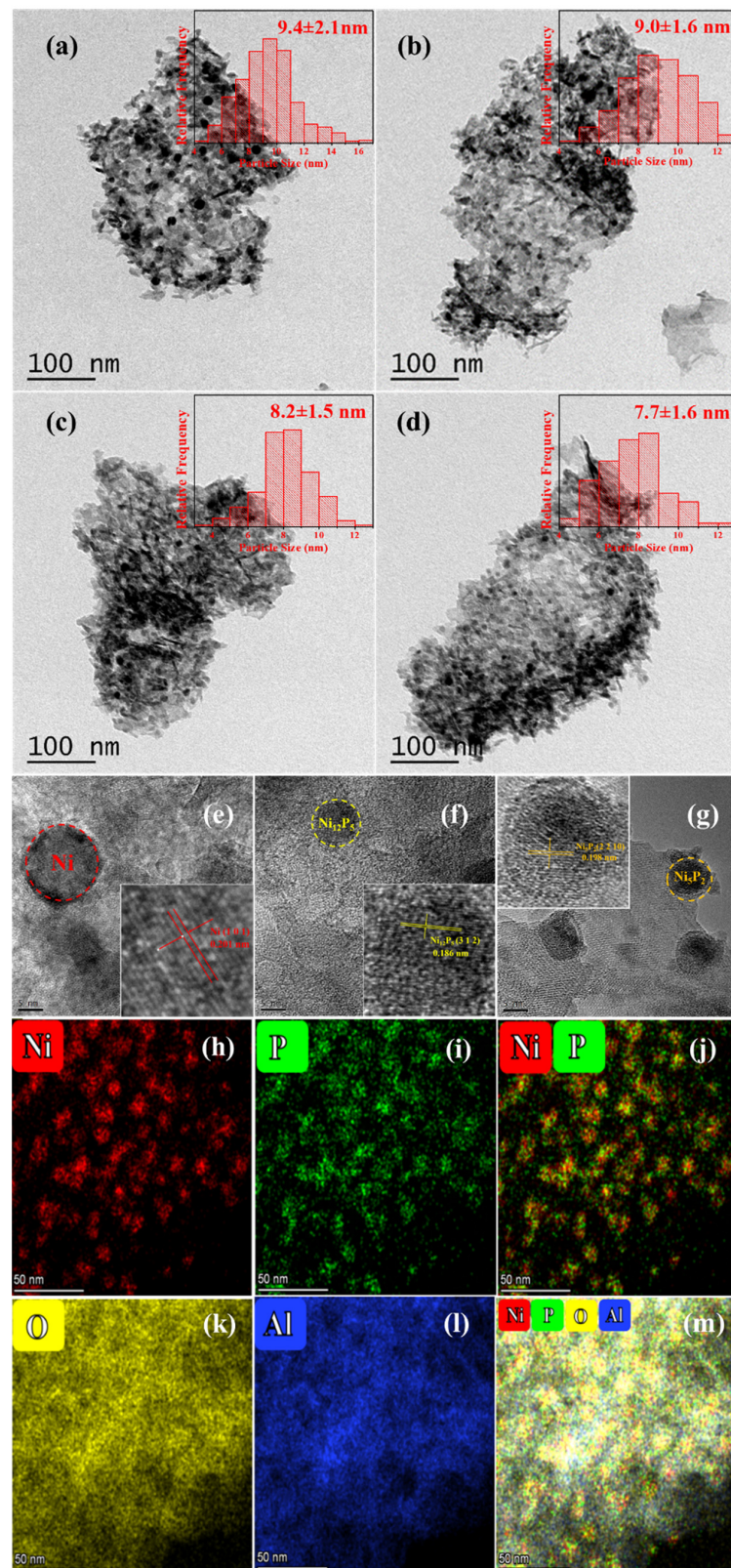


Figure 2. TEM images and corresponding size distributions of reduced (a) Ni/Al₂O₃; (b) NiP-4/Al₂O₃; (c) NiP-3/Al₂O₃; (d) NiP-2/Al₂O₃; (e–g) HRTEM image (the inset is the magnified image of Ni, Ni₁₂P₅ and Ni₅P₂) for reduced NiP-2/Al₂O₃ catalyst; and (h–m) elemental mapping results for reduced NiP-2/Al₂O₃ catalyst.

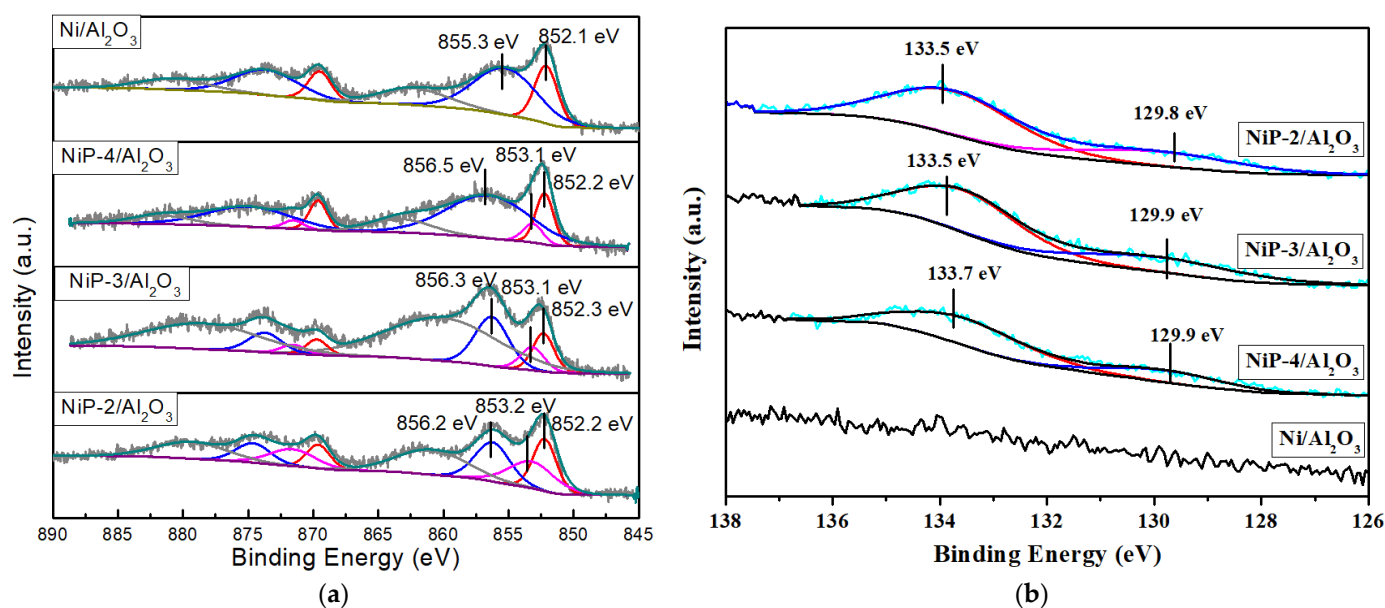


Figure 3. (a) Ni 2p and (b) P 2p XPS spectra of reduced Ni/Al₂O₃ and NiP-x/Al₂O₃ catalysts.

Table 2. Ni species distribution (Ni^{X+}/Ni ratio) of reduced Ni/Al₂O₃ and NiP-x/Al₂O₃ catalysts.

Catalyst		Nickel Species Distribution		
		Ni ⁰	Ni ^{δ+}	Ni ²⁺
Ni/Al ₂ O ₃	Position (eV)	852.1	-	855.3
	Species distribution	29.1	0	70.9
NiP-4/Al ₂ O ₃	Position (eV)	852.2	853.1	856.5
	Species distribution	18.8	7.7	73.5
NiP-3/Al ₂ O ₃	Position (eV)	852.3	853.2	856.3
	Species distribution	26.8	18.5	54.7
NiP-2/Al ₂ O ₃	Position (eV)	852.2	853.2	856.2
	Species distribution	32.0	32.4	35.6

H₂-TPR measurements were employed to investigate the interaction between Ni, P species, and alumina support of the calcined catalysts. Unsupported bulk NiO is known to be reduced to metallic Ni in the 200–450 °C range [33,44]. However, as is shown in Figure 4, the main reduction peak of nickel shifted to 700 to 900 °C temperature range, which may be due to the strong interaction between NiO and alumina support. These strong NiO-Al₂O₃ interactions are caused by the dissolution and incorporation of Al³⁺ ions in NiO crystallites [44,45]. A new shoulder peak at temperature range of 900–1000 °C, corresponding to the formation of AlPO₄ [38,46], along with an obvious shift to higher temperature of the main nickel species peaks are observed for the P-containing catalysts, which implies that the presence of P results in stronger metal–support interaction between nickel and alumina support.

NH₃-TPD was performed to investigate the acidic property of the samples. Figure 5 shows the NH₃-TPD profiles of Al₂O₃ supported catalysts reduced at 900 °C. γ-Al₂O₃ support has been also tested in order to better define the effect of phosphorous on surface acidity. For the reference alumina support, three main NH₃ desorption peaks centered at ~123 °C, ~259 °C, and ~587 °C, which are associated with weak, medium, and strong acid sites, respectively, are identified. It is noted that evident decrease of peak area of Ni/Al₂O₃ NH₃-TPD profiles is observed in comparison with the reference Al₂O₃, which indicates that nickel could weaken the surface acidity. What is more, obvious peak area decreases

for the phosphorus presence catalysts, which suggests that phosphorus could decrease the surface acidity on Ni/Al₂O₃ catalyst.

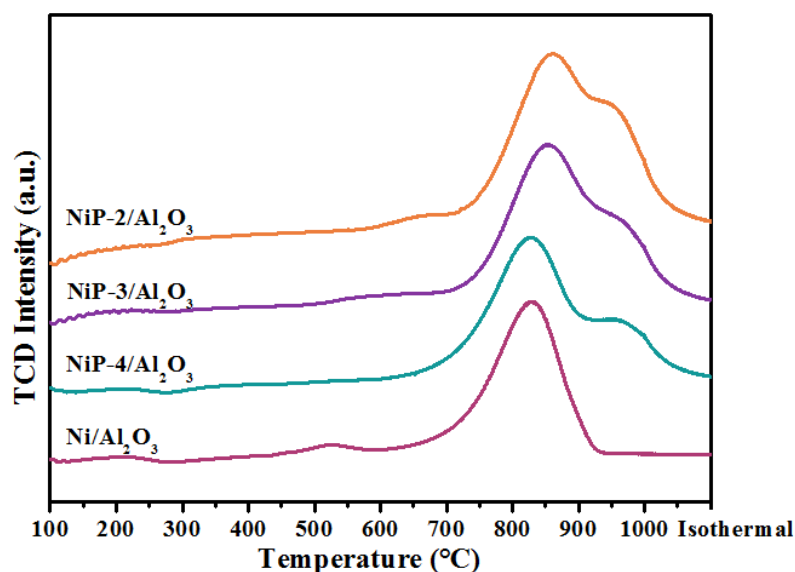


Figure 4. H₂-TPR profiles of reduced Ni/Al₂O₃ and NiP-x/Al₂O₃ catalysts.

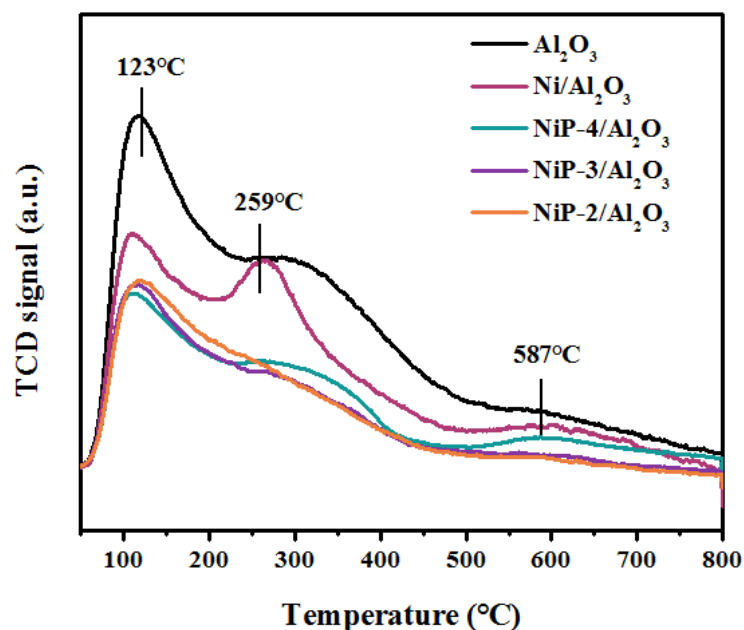


Figure 5. NH₃-TPD profiles of reduced Ni/Al₂O₃ and NiP-x/Al₂O₃ catalysts.

3.2. Catalytic Performance

Dry methane reforming results with time on stream for 50 h, which were performed over reduced catalysts at 700 °C, CH₄:CO₂:N₂ = 1:1:1, the WHSV = 18,000 mL gcat⁻¹ h⁻¹, ambient atmosphere, are shown in Figure 6. As is indicated, the Ni/Al₂O₃ catalyst exhibits excellent catalytic performance. The methane and carbon dioxide conversion are as high as 80% and 87%, which is close to the equilibrium conversion. The higher CO₂ conversion than methane conversion may be due to the simultaneous occurrence of the reverse water gas shift reaction (CO₂ + H₂ = H₂O + CO) [47], which is also the reason for lower H₂/CO ratio than stoichiometric amount. A slight decrease of activity is observed for the P presence catalysts in dry methane reforming. This decrease of activity is probably partially due to both the partial coverage of metallic nickel by phosphorus species and less metallic nickel

as the existence of nickel phosphides species. Note that no further activity decrease is observed with the increasing phosphorus content at our study range.

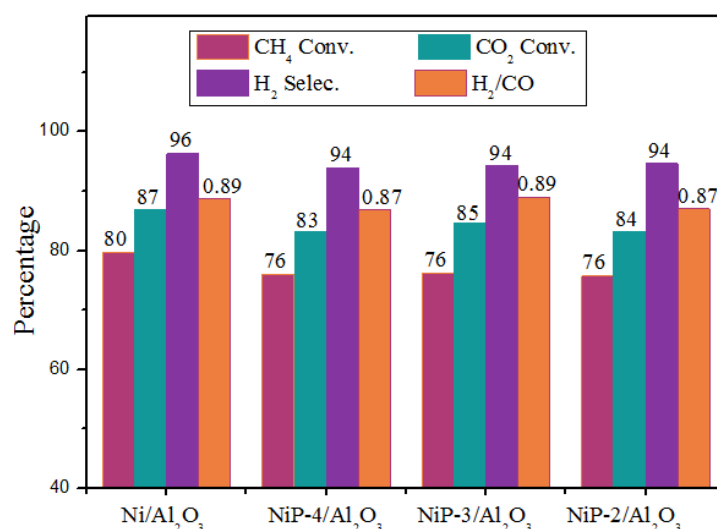


Figure 6. Catalytic performance of Ni/Al₂O₃ and NiP-x/Al₂O₃ catalysts in dry methane reforming.

For further study, the stability of Ni/Al₂O₃ and NiP-x/Al₂O₃ catalysts was investigated for at least 50 h and the results are shown in Figure 7. It is indicated that an activity degradation is observed within the 50 h of time on stream over Ni/Al₂O₃ catalyst. The CH₄ and CO₂ conversion dropped from 80% and 87% to 76% and 84%, respectively. The activity degradation may be due to the surface carbon deposition and/or particle sintering, which are common reasons for activity degradation over nickel-based catalysts during dry methane reforming process. It is worth pointing out that all the P presence catalysts exhibited better stability than Ni/Al₂O₃ catalyst during dry methane reforming. No visible activity loss was observed within 50 h of time on stream.

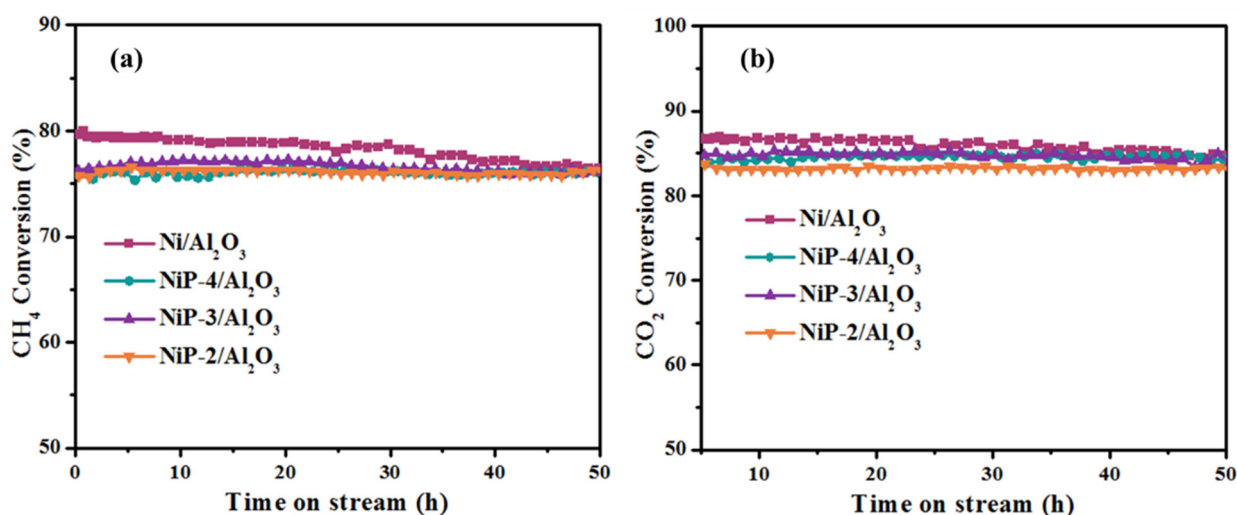


Figure 7. (a) CH₄ and (b) CO₂ conversion as a function of time on stream over Ni/Al₂O₃ and NiP-x/Al₂O₃ catalysts.

3.3. Characterization of Spent Catalysts

TG analyses were performed on the spent catalysts after 50 h DMR reaction to determine the amount of carbon deposition. As is shown in Figure 8, all the spent catalysts exhibit several weight changes in temperature range of 30–800 °C. The first weight loss below 200 °C can be associated with the removal of physically adsorbed H₂O, while the

tiny weight gain between 240–360 °C can be attributed to oxidation of the metallic Ni to its corresponding oxides [48]. The second weight loss at 450–700 °C can be ascribed to the oxidation of graphitic carbon deposited on the catalyst during the DMR reaction [49,50]. No evident weight loss is observed in the temperature range of 240–360 °C, attributed to the oxidation of surface amorphous carbon [49]. This implies that the generation graphitic carbon is the main reason for carbon deposition, which coincides with the literature. Note that obvious less weight loss at 450–700 °C is observed for the phosphorus presence catalysts and the content of carbon deposition decreases in the following order: Ni/Al₂O₃ (34.8%) > NiP-4/Al₂O₃ (21.8%) > NiP-3/Al₂O₃ (17.5%) > NiP-2/Al₂O₃ (2.7%), which is in line with the intensity trend of the graphitic carbon diffraction peak in the XRD patterns (Figure 9). The result strongly implies that the existence of P species results in better resistance of carbon deposition over the catalysts during dry methane reforming process. The enhancement of carbon deposition resistance of P presence catalysts might be one of the reasons for better stability in dry methane reforming. The tendency indicates that when the amount of P increases, the degree of carbon deposited on the surface of the catalyst decreases.

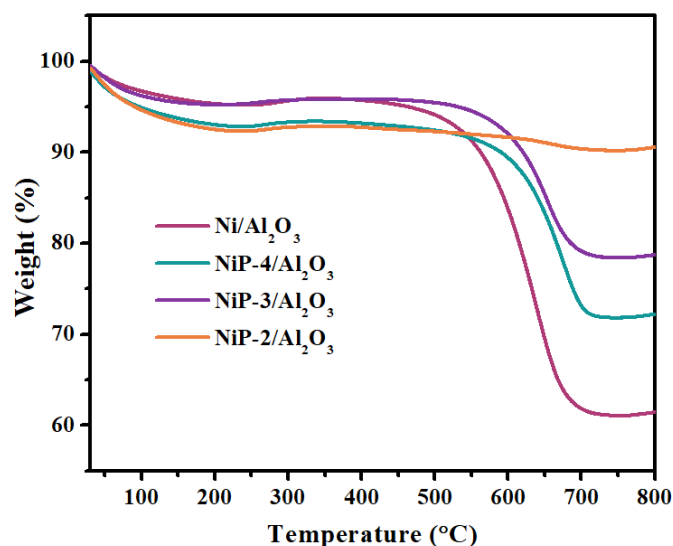


Figure 8. TG profiles of spent Ni/Al₂O₃ and NiP-x/Al₂O₃ catalysts.

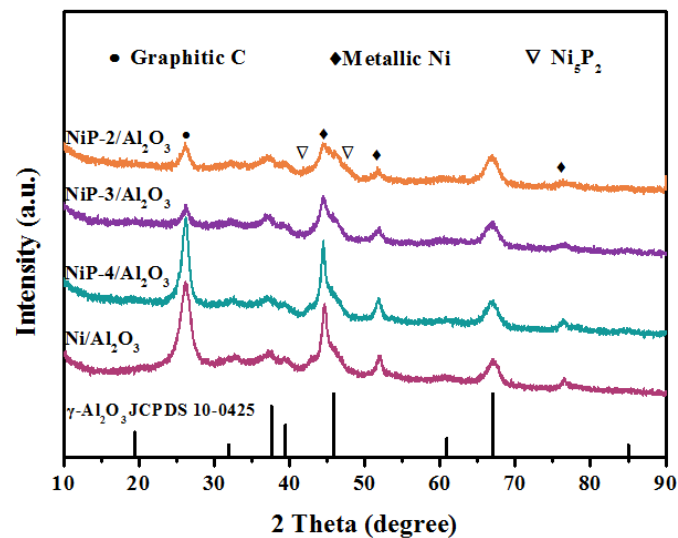


Figure 9. XRD patterns of spent Ni/Al₂O₃ and NiP-x/Al₂O₃ catalysts.

The XRD patterns of spent Al_2O_3 supported catalysts are shown in Figure 9. Compared with the fresh catalysts, the relative sharp peaks shape of metallic nickel and nickel phosphides species indicates the growth of crystalline size during dry methane reforming at high temperature. Phosphorus-contained catalysts indicate relative wide peaks of nickel species, implying better anti-sintering properties compared to $\text{Ni}/\text{Al}_2\text{O}_3$ catalyst. Characteristic peak at 2θ of 26.2° , attributed to graphitic carbon due to the carbon deposition during dry methane reforming process, is detected over all the catalysts. Note that relative peak intensity of $\text{NiP-x}/\text{Al}_2\text{O}_3$, especially for the $\text{NiP-3}/\text{Al}_2\text{O}_3$ and $\text{NiP-2}/\text{Al}_2\text{O}_3$, decreases obviously, indicating less carbon deposition, which coincides with the TG result.

TEM images and particle size distributions of the spent catalysts are shown in Figure S2. The particle size distributions of catalysts before and after the DMR reaction are summarized in Table 3. As is shown in the TEM images, obvious filamentous carbon species are observed encapsulating on $\text{Ni}/\text{Al}_2\text{O}_3$ catalyst, indicating the severe carbon deposition, which is also confirmed by TG profiles and XRD patterns. As is depicted in Table 3, a small enhancement of particle sizes of nickel species is observed for all the spent catalysts, which coincides with the XRD result. Note that the enhancing range of nickel species particle size is obviously restrained for the phosphorus presence catalysts. This result further implies that the presence of phosphorus increases the anti-sintering properties of nickel catalyst.

Table 3. Particle size distributions of fresh and spent $\text{Ni}/\text{Al}_2\text{O}_3$ and $\text{NiP-x}/\text{Al}_2\text{O}_3$ catalysts.

Catalyst	Particle Size Distribution (nm)		Particle Size Enhancing Range (%)
	Fresh Catalysts	Spent Catalysts	
$\text{Ni}/\text{Al}_2\text{O}_3$	9.4 ± 2.1	10.3 ± 2.5	9.6
$\text{NiP-4}/\text{Al}_2\text{O}_3$	9.0 ± 1.6	9.5 ± 1.5	5.6
$\text{NiP-3}/\text{Al}_2\text{O}_3$	8.2 ± 1.5	8.5 ± 1.4	3.7
$\text{NiP-2}/\text{Al}_2\text{O}_3$	7.7 ± 1.6	8.4 ± 1.8	9.1

3.4. DRIFTS Analysis

In-situ CO_2 adsorption diffuse reflectance infrared Fourier transform spectroscopy (DRIFTS) analyses were carried out to obtain information about the plausible DMR reaction mechanism and Figure S3, Figure 10 recorded spectra. The bands between $2250\text{--}2450\text{ cm}^{-1}$ can be assigned to CO_2 species, whose relative concentration changes with temperature. At 50°C , the band at 2344 cm^{-1} , together with two bands localized at 3700 and 3600 cm^{-1} , are observed on the spectra for both catalysts, and can be attributed to the gas phase CO_2 [11,51–54]. At higher temperature, new bands at 2386 , 2377 , 2332 , 2319 , 2309 , 2294 , and 2284 cm^{-1} are observed, and can be attributed to the chemisorbed species of CO_2 on the Lewis acid sites of alumina support [55,56]. Note that obvious depletion of CO_2 overtones at bands of 2344 , 3600 , and 3700 cm^{-1} [51,53], along with the enhanced intensity of the bands, belong to adsorbed CO_2 species and are observed with the increasing temperature. This result implies that higher temperature is favorable for the chemisorption of CO_2 over the catalysts.

The bands between $1800\text{--}1200\text{ cm}^{-1}$ indicate the formation of adsorbed C-containing species on the catalyst surface during reaction, whose relative concentration changes with temperature. At 50°C , both spectra show bands at 1652 and 1430 cm^{-1} that can be assigned to O–C–O stretching (ν_{OCO} , both symmetric and asymmetric) of bicarbonate species [51,53]. These species are formed by protonation of carbonate species with alkaline hydroxyl OH^* active species. The O–H stretching bands of these bicarbonates is also observed at 3725 and 3625 cm^{-1} . Moreover, the band at 1562 cm^{-1} can be attributed to the asymmetric O–C–O stretching which is the characteristic band of formate species adsorbed on Al_2O_3 . The formate species, formed by the further evolution of bicarbonate species, are one of the possible reaction intermediates, and could further yield CO. Besides, the tiny bands at 2931 and 2862 cm^{-1} , related to the CH_x stretching mode of formats, confirms the presence of

these species. The formate species, created by the further evolution of bicarbonate species, are one of the possible reaction intermediates, and could further yield CO. The existence of gas phase CO is proved by the tiny band at around 2230 cm^{-1} at higher temperature. With the increase of temperatures, evidence the depletion of bicarbonates and the formation of formates are observed for both catalysts. The evolution of bands with temperature suggests that CO_2 proceeds via formation of carbonyl species, mainly arising from intermediate formates decomposition to CO during dry methane reforming.

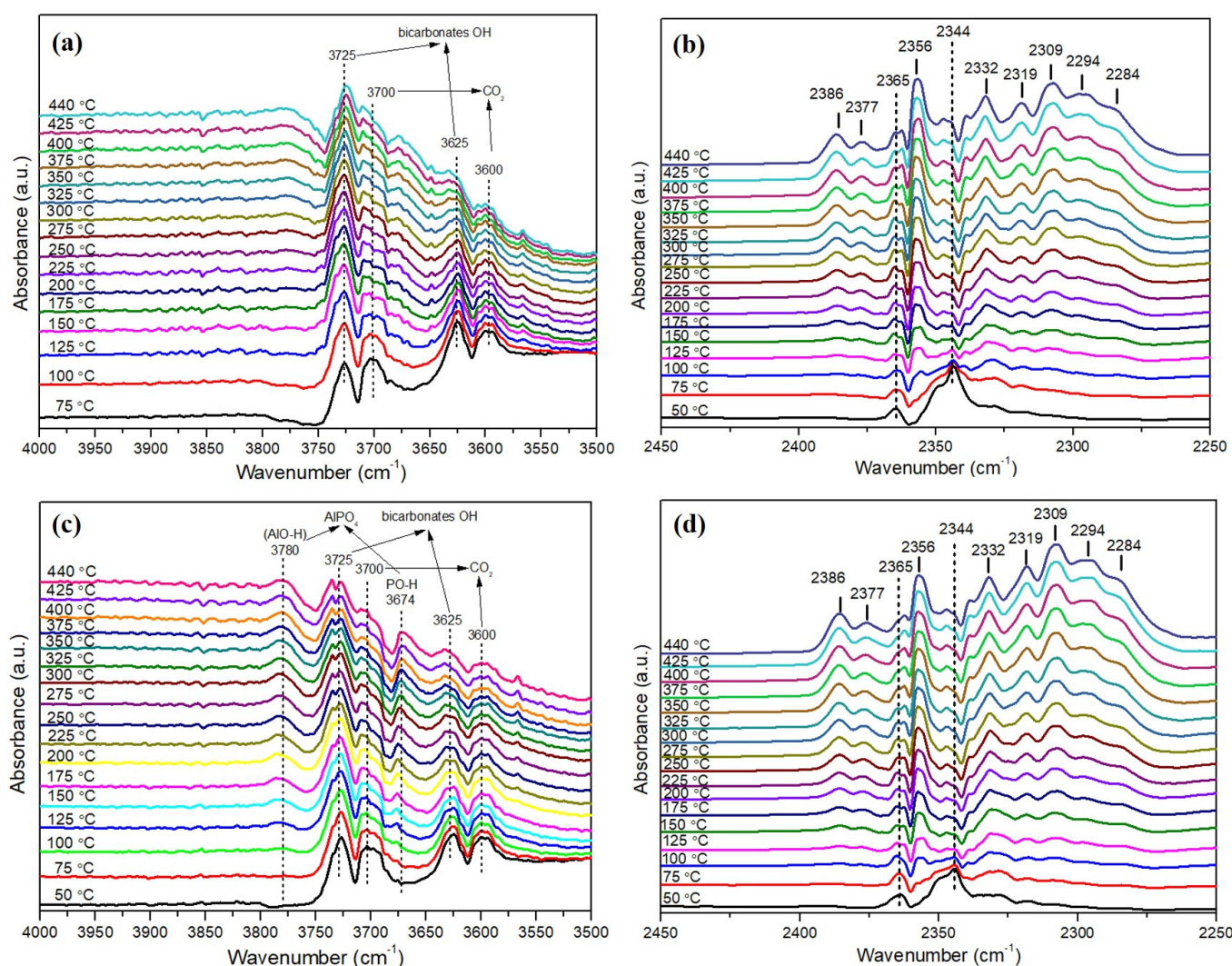


Figure 10. Partial DRIFT spectra of CO_2 adsorbed at different temperatures over $\text{Ni}/\text{Al}_2\text{O}_3$ with the wavelength $3500\text{--}4000\text{ cm}^{-1}$ (a), $2250\text{--}2450\text{ cm}^{-1}$ (b), and over $\text{NiP-2}/\text{Al}_2\text{O}_3$ catalyst with the wavelength $3500\text{--}4000\text{ cm}^{-1}$ (c), $2250\text{--}2450\text{ cm}^{-1}$ (d).

Note that two new bands at 3780 and 3674 cm^{-1} are observed over $\text{NiP-2}/\text{Al}_2\text{O}_3$ catalyst, which can be attributed to the hydroxyl groups of AlO-H and PO-H species, respectively, belonging to the AlPO_4 phase [57–59]. The existence of AlPO_4 phase is also confirmed by H_2 -TPR and XPS spectra. These hydroxyl groups might benefit for the adsorption of CO_2 on catalyst during reaction.

Compared to $\text{Ni}/\text{Al}_2\text{O}_3$, the spectrum of $\text{NiP-2}/\text{Al}_2\text{O}_3$ presents evident higher intensity of the bands of adsorbed CO_2 species, which implies the higher CO_2 adsorption ability of $\text{NiP-2}/\text{Al}_2\text{O}_3$ catalyst. Additionally, lower bicarbonates bands at 1652 and 1430 cm^{-1} and higher formates species bands at 1562 , 2931 , and 2862 cm^{-1} over $\text{NiP-2}/\text{Al}_2\text{O}_3$ catalyst are also observed. This result indicates that phosphorus presence catalysts

own better activation ability of CO₂. The produced bicarbonates species are more easily further converted to formate intermediates and active O* species, which favors the elimination of the carbon deposition.

4. Discussion

It is known that nickel catalyst shows excellent catalytic activity in dry methane reforming. However, due to the relative higher CH₄ dissociation ability of nickel catalysts, severe carbon deposition restricts its application. Previous reports indicated that the transition metal phosphides expressed excellent catalytic performance and carbon deposition resistance for dry methane reforming. Nevertheless, due to the relative higher CO₂ dissociation ability of transition metal phosphides, oxidation of phosphides to phosphate phase was also observed at high temperature and GHSV condition during dry methane reforming. In this work, the strong CH₄ dissociation ability of metallic nickel and excellent CO₂ dissociation ability of nickel phosphides were combined to obtain better carbon deposition resistance.

A series of NiP-x/Al₂O₃ catalysts containing different ratio of metallic nickel to nickel phosphides were prepared by varying Ni/P molar ratio of 4, 3, 2 through a co-impregnation method. The obtained results reveal an evident influence of phosphorus content on the catalyst structure and the catalytic performances in dry methane reforming. ICP results indicate that the measured contents of nickel and phosphorus roughly match with their nominal values, which implies no visible mass loss of phosphorus during reduction at high temperatures. XRD and TEM suggest that nickel is highly dispersed on the alumina surface support and the P presence catalysts exhibit smaller nickel particle size. The co-existence of metallic nickel and nickel phosphides phase is confirmed by XRD, XPS, and HRTEM images. Moreover, nickel species are prone to enrich the phosphorus existence place, which is confirmed by element mapping analysis. H₂-TPR highlights strong interaction between nickel and alumina support for non-promoted samples after calcination. The addition of phosphorus is supposed to reinforce this interaction between nickel and alumina support.

As expected, Ni/Al₂O₃ catalyst shows good activity while having a slight deactivation after 50 h of time on stream in dry methane reforming. XRD data of the spent Ni/Al₂O₃ sample reveals the enhancement of nickel crystallite size. Moreover, severe carbon deposition and nickel particle size enhancement are detected by TG, XRD, and TEM analyses. The increase of nickel particle size and carbon deposition should be the reasons for the slight deactivation. The phosphorus containing catalysts exhibit slight lower activity while showing better stability in dry methane reforming. Obvious lower carbon deposition and particle size increase are detected by TG and TEM analyses over the spent P-containing catalysts. In addition, in-situ CO₂ adsorption DRIFTS analysis gives information that the phosphorus containing catalysts own evident higher CO₂ adsorption and dissociation ability, which coincides with the publications [36,41]. The better CO₂ dissociation ability and anti-sintering property should be responsible for the better anti-coking and stability of the phosphorus containing catalysts. Note that the carbon deposition is strongly influenced by the phosphorus content. The NiP-2/Al₂O₃ catalyst exhibits best resistance of carbon deposition, which may be due to the better balance between CH₄ dissociation and CO₂ dissociation over the catalyst during dry methane reforming.

5. Conclusions

A series of NiP-x/Al₂O₃ catalysts containing different ratios of metallic nickel to nickel phosphides, prepared by varying Ni/P molar ratio of 4, 3, 2 through a co-impregnation method, were employed to investigate the synergistic effect of metallic nickel–nickel phosphides in dry methane reforming reaction. Good dispersion of nickel particles and strong nickel-alumina interaction is confirmed by a series of characterizations over the P-free catalyst. In addition, the Ni/Al₂O₃ catalyst indicates good activity but severe carbon deposition in dry methane reforming reaction.

The presence of phosphorus increases nickel dispersion as well as the interaction between nickel and alumina support, which results in smaller nickel particles. The co-

existence of metallic nickel and nickel phosphides species is confirmed. Moreover, compared to the Ni/Al₂O₃ catalyst, phosphorus contained catalysts exhibit higher CO₂ dissociation ability. Due to the relative stronger CO₂ dissociation ability, NiP-x/Al₂O₃ catalysts indicate obvious higher resistance of carbon deposition. Furthermore, because of good balance between CH₄ dissociation and CO₂ dissociation, NiP-2/Al₂O₃ catalyst exhibits best resistance of carbon deposition, and few carbon depositions were formed after 50 h of dry methane reforming.

Supplementary Materials: The following supporting information can be downloaded at: <https://www.mdpi.com/article/10.3390/ma15093044/s1>, Figure S1: HRTEM image of the reduced Ni/Al₂O₃ catalysts (the inset is the magnified image of Ni); Figure S2: TEM images and corresponding size distributions of spent (a) Ni/Al₂O₃; (b) NiP-4/Al₂O₃; (c) NiP-3/Al₂O₃; (d) NiP-2/Al₂O₃; Figure S3: DRIFTS spectra of CO₂ temperature programmed adsorption at different temperatures over (a) Ni/Al₂O₃ and (b) NiP-2/Al₂O₃.

Author Contributions: Conceptualization, T.L. and H.Y. (Hongfeng Yin); methodology, T.L.; validation, Y.S., S.W. and Y.L.; formal analysis, Y.S.; investigation, Y.S., F.Y., Y.C. and H.Y. (Hongbo Yu); data curation, Y.S. and T.L.; writing—original draft preparation, Y.S.; writing—review and editing, T.L. and H.Y. (Hongfeng Yin); visualization, Y.S.; supervision, H.Y. (Hongfeng Yin); project administration, H.Y. (Hongfeng Yin); funding acquisition, S.W. All authors have read and agreed to the published version of the manuscript.

Funding: This research was funded by the Postdoctoral Science Preferential Funding of Zhejiang Province, grant number ZJ2020005.

Institutional Review Board Statement: Not applicable.

Informed Consent Statement: Not applicable.

Data Availability Statement: Not applicable.

Conflicts of Interest: The authors declare no conflict of interest.

References

1. Ashcroft, A.; Cheetham, A.; Green, M. Partial oxidation of methane to synthesis gas using carbon dioxide. *Nature* **1991**, *352*, 225–226. [[CrossRef](#)]
2. Arman, A.; Hagos, F.Y.; Abdullah, A.A.; Mamat, R.; Aziz, A.R.A.; Cheng, C.K. Syngas production through steam and CO₂ reforming of methane over Ni-based catalyst—A Review. *IOP Conf. Ser. Mater. Sci. Eng.* **2020**, *736*, 042032. [[CrossRef](#)]
3. Song, Y.; Ozdemir, E.; Ramesh, S.; Adishev, A.; Subramanian, S.; Harale, A.; Albuali, M.; Fadhel, B.A.; Jamal, A.; Moon, D. Dry reforming of methane by stable Ni–Mo nanocatalysts on single-crystalline MgO. *Science* **2020**, *367*, 777–781. [[CrossRef](#)] [[PubMed](#)]
4. Hengyong, X.; Xixian, S.; Yemei, F.; Guolin, X.; Jinxiang, L.; Wenge, Y.; Peiheng, Z. Studies of Reforming Methane with Carbon Dioxide to Produce Synthesis Gas I. Catalyst and Its Catalytic Property. *Petrochem. Technol.* **1992**, *3*, 1.
5. Jang, W.-J.; Shim, J.-O.; Kim, H.-M.; Yoo, S.-Y.; Roh, H.-S. A review on dry reforming of methane in aspect of catalytic properties. *Catal. Today* **2019**, *324*, 15–26. [[CrossRef](#)]
6. Wang, N.; Shen, K.; Huang, L.; Yu, X.; Qian, W.; Chu, W. Facile Route for Synthesizing Ordered Mesoporous Ni–Ce–Al Oxide Materials and Their Catalytic Performance for Methane Dry Reforming to Hydrogen and Syngas. *ACS Catal.* **2013**, *3*, 1638–1651. [[CrossRef](#)]
7. Goula, M.; Lemonidou, A.; Efstathiou, A.M. Characterization of Carbonaceous Species Formed during Reforming of CH₄ with CO₂ over Ni/CaO–Al₂O₃ Catalysts Studied by Various Transient Techniques. *J. Catal.* **1996**, *161*, 626–640. [[CrossRef](#)]
8. Arora, S.; Prasad, R. An overview on dry reforming of methane: Strategies to reduce carbonaceous deactivation of catalysts. *RSC Adv.* **2016**, *6*, 108668–108688. [[CrossRef](#)]
9. Shen, J.; Reule, A.A.C.; Semagina, N. Ni/MgAl₂O₄ catalyst for low-temperature oxidative dry methane reforming with CO₂. *Int. J. Hydrog. Energy* **2019**, *44*, 4616–4629. [[CrossRef](#)]
10. Zanganeh, R.; Rezaei, M.; Zamaniyan, A. Dry reforming of methane to synthesis gas on NiO–MgO nanocrystalline solid solution catalysts. *Int. J. Hydrog. Energy* **2013**, *38*, 3012–3018. [[CrossRef](#)]
11. Lin, S.; Wang, J.; Mi, Y.; Yang, S.; Wang, Z.; Liu, W.; Wu, D.; Peng, H. Trifunctional strategy for the design and synthesis of a Ni–CeO₂@SiO₂ catalyst with remarkable low-temperature sintering and coking resistance for methane dry reforming. *Chin. J. Catal.* **2021**, *42*, 1808–1820. [[CrossRef](#)]
12. Li, K.; Chang, X.; Pei, C.; Li, X.; Chen, S.; Zhang, X.; Assabumrungrat, S.; Zhao, Z.-J.; Zeng, L.; Gong, J. Ordered mesoporous Ni/La₂O₃ catalysts with interfacial synergism towards CO₂ activation in dry reforming of methane. *Appl. Catal. B Environ.* **2019**, *259*, 118092. [[CrossRef](#)]

13. Wang, J.; Fu, Y.; Kong, W.; Jin, F.; Bai, J.; Zhang, J.; Sun, Y. Design of a carbon-resistant Ni@S-2 reforming catalyst: Controllable Ni nanoparticles sandwiched in a peasecod-like structure. *Appl. Catal. B Environ.* **2021**, *282*, 119546. [[CrossRef](#)]
14. Świrk, K.; Gálvez, M.E.; Motak, M.; Grzybek, T.; Rønning, M.; Costa, P.D. Syngas production from dry methane reforming over yttrium-promoted nickel-KIT-6 catalysts. *Int. J. Hydrog. Energy* **2019**, *44*, 274–286. [[CrossRef](#)]
15. Han, B.; Wang, F.; Zhang, L.; Wang, Y.; Fan, W.; Xu, L.; Yu, H.; Li, Z. Syngas production from methane steam reforming and dry reforming reactions over sintering-resistant Ni@SiO₂ catalyst. *Res. Chem. Intermed.* **2020**, *46*, 1735–1748. [[CrossRef](#)]
16. Liu, W.; Li, L.; Zhang, X.; Wang, Z.; Wang, X.; Peng, H. Design of Ni-ZrO₂@SiO₂ catalyst with ultra-high sintering and coking resistance for dry reforming of methane to prepare syngas. *J. CO₂ Util.* **2018**, *27*, 297–307. [[CrossRef](#)]
17. Boukha, Z.; Jiménez-González, C.; Rivas, B.D.; González-Velasco, J.R.; Gutiérrez-Ortiz, J.I.; López-Fonseca, R. Synthesis, characterisation and performance evaluation of spinel-derived Ni/Al₂O₃ catalysts for various methane reforming reactions. *Appl. Catal. B Environ.* **2014**, *158*, 190–201. [[CrossRef](#)]
18. Cho, E.; Lee, Y.-H.; Kim, H.; Jang, E.J.; Kwak, J.H.; Lee, K.; Ko, C.H.; Yoon, W.L. Ni catalysts for dry methane reforming prepared by A-site exsolution on mesoporous defect spinel magnesium aluminate. *Appl. Catal. A Gen.* **2020**, *602*, 117694. [[CrossRef](#)]
19. Sierra Gallego, G.; Batiot-Dupeyrat, C.; Barrault, J.; Mondragón, F. Dual Active-Site Mechanism for Dry Methane Reforming over Ni/La₂O₃ Produced from LaNiO₃ Perovskite. *Ind. Eng. Chem. Res.* **2008**, *47*, 9272–9278. [[CrossRef](#)]
20. Gallego, G.S.; Marín, J.G.; Batiot-Dupeyrat, C.; Barrault, J.; Mondragón, F. Influence of Pr and Ce in dry methane reforming catalysts produced from La_{1-x}A_xNiO_{3-δ} perovskites. *Appl. Catal. A Gen.* **2009**, *369*, 97–103. [[CrossRef](#)]
21. Joo, S.; Seong, A.; Kwon, O.; Kim, K.; Lee, J.H.; Gorte, R.J.; Vohs, J.M.; Han, J.W.; Kim, G. Highly active dry methane reforming catalysts with boosted in situ grown Ni-Fe nanoparticles on perovskite via atomic layer deposition. *Sci. Adv.* **2020**, *6*, eabb1573. [[CrossRef](#)] [[PubMed](#)]
22. Debek, R.; Galvez, M.E.; Launay, F.; Motak, M.; Grzybek, T.; Costa, P.D. Low temperature dry methane reforming over Ce, Zr and CeZr promoted Ni–Mg–Al hydrotalcite-derived catalysts. *Int. J. Hydrog. Energy* **2016**, *41*, 11616–11623. [[CrossRef](#)]
23. Debek, R.; Motak, M.; Galvez, M.E.; Grzybek, T.; Costa, P.D. Promotion effect of zirconia on Mg(Ni,Al)O mixed oxides derived from hydrotalcites in CO₂ methane reforming. *Appl. Catal. B Environ.* **2018**, *223*, 36–46. [[CrossRef](#)]
24. Liu, H.; Wierzbicki, D.; Debek, R.; Motak, M.; Grzybek, T.; Costa, P.D.; Gálvez, M.E. La-promoted Ni-hydrotalcite-derived catalysts for dry reforming of methane at low temperatures. *Fuel* **2016**, *182*, 8–16. [[CrossRef](#)]
25. Danghyan, V.; Kumar, A.; Mukasyan, A.; Wolf, E.E. An active and stable NiOMgO solid solution based catalysts prepared by paper assisted combustion synthesis for the dry reforming of methane. *Appl. Catal. B Environ.* **2020**, *273*, 119056. [[CrossRef](#)]
26. Padi, S.P.; Shelly, L.; Komarala, E.P.; Schweke, D.; Hayun, S.; Rosen, B.A. Coke-free methane dry reforming over nano-sized NiO-CeO₂ solid solution after exsolution. *Catal. Commun.* **2020**, *138*, 105951. [[CrossRef](#)]
27. Turap, Y.; Wang, I.; Fu, T.; Wu, Y.; Wang, Y.; Wang, W. Co–Ni alloy supported on CeO₂ as a bimetallic catalyst for dry reforming of methane. *Int. J. Hydrog. Energy* **2020**, *45*, 6538–6548. [[CrossRef](#)]
28. San-José-Alonso, D.; Juan-Juan, J.; Illán-Gómez, M.J.; Román-Martínez, M.C. Ni, Co and bimetallic Ni–Co catalysts for the dry reforming of methane. *Appl. Catal. A Gen.* **2009**, *371*, 54–59. [[CrossRef](#)]
29. Rostrup-Nielsen, J. Sulfur-passivated nickel catalysts for carbon-free steam reforming of methane. *J. Catal.* **1984**, *85*, 31–43. [[CrossRef](#)]
30. Brungs, A.J.; York, A.P.; Claridge, J.B.; Márquez-Alvarez, C.; Green, M.L. Dry reforming of methane to synthesis gas over supported molybdenum carbide catalysts. *Catal. Lett.* **2000**, *70*, 117–122. [[CrossRef](#)]
31. Ma, Y.; Guan, G.; Hao, X.; Cao, J.; Abudula, A. Molybdenum carbide as alternative catalyst for hydrogen production—A review. *Renew. Sustain. Energy Rev.* **2017**, *75*, 1101–1129. [[CrossRef](#)]
32. Zhang, S.; Shi, C.; Chen, B.; Zhang, Y.; Zhu, Y.; Qiu, J.; Au, C. Catalytic role of β-Mo₂C in DRM catalysts that contain Ni and Mo. *Catal. Today* **2015**, *258*, 676–683. [[CrossRef](#)]
33. Shi, C.; Zhang, S.; Li, X.; Zhang, A.; Shi, M.; Zhu, Y.; Qiu, J.; Au, C. Synergism in NiMoO_x precursors essential for CH₄/CO₂ dry reforming. *Catal. Today* **2014**, *233*, 46–52. [[CrossRef](#)]
34. Cheng, J.; Huang, W. Effect of cobalt (nickel) content on the catalytic performance of molybdenum carbides in dry-methane reforming. *Fuel Processing Technol.* **2010**, *91*, 185–193. [[CrossRef](#)]
35. Yao, Z.; Luan, F.; Sun, Y.; Jiang, B.; Song, J.; Wang, H. Molybdenum phosphide as a novel and stable catalyst for dry reforming of methane. *Catal. Sci. Technol.* **2016**, *6*, 7996–8004. [[CrossRef](#)]
36. Cui, Y.; Liu, Q.; Yao, Z.; Dou, B.; Shi, Y.; Sun, Y. A comparative study of molybdenum phosphide catalyst for partial oxidation and dry reforming of methane. *Int. J. Hydrog. Energy* **2019**, *44*, 11441–11447. [[CrossRef](#)]
37. González-Castaño, M.; Saché, E.L.; Berry, C.; Pastor-Pérez, L.; Arellano-García, H.; Wang, Q.; Reina, T.R. Nickel Phosphide Catalysts as Efficient Systems for CO₂ Upgrading via Dry Reforming of Methane. *Catalysts* **2021**, *11*, 446. [[CrossRef](#)]
38. Bang, S.; Hong, E.; Baek, S.W.; Shin, C.-H. Effect of acidity on Ni catalysts supported on P-modified Al₂O₃ for dry reforming of methane. *Catal. Today* **2018**, *303*, 100–105. [[CrossRef](#)]
39. Wang, N.; Qian, W.; Chu, W.; Wei, F. Crystal-plane effect of nanoscale CeO₂ on the catalytic performance of Ni/CeO₂ catalysts for methane dry reforming. *Catal. Sci. Technol.* **2016**, *6*, 3594–3605. [[CrossRef](#)]
40. Jiménez-Gómez, C.P.; Cecilia, J.A.; Moreno-Tost, R.; Maireles-Torres, P. Nickel Phosphide/Silica Catalysts for the Gas-Phase Hydrogenation of Furfural to High-Added-Value Chemicals. *ChemCatChem* **2017**, *9*, 2881–2889. [[CrossRef](#)]

41. Wu, W.; Liu, Q.; Shi, Y.; Yao, Z.; Ding, W.; Dou, B. Binary and ternary transition metal phosphides for dry reforming of methane. *React. Chem. Eng.* **2020**, *5*, 719–727. [[CrossRef](#)]
42. Zeng, Y.; Ma, H.; Zhang, H.; Ying, W.; Fang, D. Highly efficient NiAl₂O₄-free Ni/ γ -Al₂O₃ catalysts prepared by solution combustion method for CO methanation. *Fuel* **2014**, *137*, 155–163. [[CrossRef](#)]
43. Li, T.; Virginie, M.; Khodakov, A.Y. Effect of potassium promotion on the structure and performance of alumina supported carburized molybdenum catalysts for Fischer-Tropsch synthesis. *Appl. Catal. A Gen.* **2017**, *542*, 154–162. [[CrossRef](#)]
44. Youn, M.H.; Seo, J.G.; Kim, P.; Song, I.K. Role and effect of molybdenum on the performance of Ni-Mo/ γ -Al₂O₃ catalysts in the hydrogen production by auto-thermal reforming of ethanol. *J. Mol. Catal. A Chem.* **2007**, *261*, 276–281. [[CrossRef](#)]
45. Malaibari, Z.O.; Croiset, E.; Amin, A.; Epling, W. Effect of interactions between Ni and Mo on catalytic properties of a bimetallic Ni-Mo/Al₂O₃ propane reforming catalyst. *Appl. Catal. A Gen.* **2015**, *490*, 80–92. [[CrossRef](#)]
46. Bang, Y.; Han, S.J.; Yoo, J.; Park, S.; Choi, J.H.; Lee, Y.J.; Song, J.H.; Song, I.K. Hydrogen production by steam reforming of liquefied natural gas (LNG) over mesoporous nickel-phosphorus-alumina aerogel catalyst. *Int. J. Hydrog. Energy* **2014**, *39*, 4909–4916. [[CrossRef](#)]
47. Xu, Z.; Wang, N.; Chu, W.; Deng, J.; Luo, S. In situ controllable assembly of layered-double-hydroxide-based nickel nanocatalysts for carbon dioxide reforming of methane. *Catal. Sci. Technol.* **2015**, *5*, 1588–1597. [[CrossRef](#)]
48. Chen, W.F.; Wang, C.H.; Sasaki, K.; Marinkovic, N.; Xu, W.; Muckerman, J.T.; Zhu, Y.; Adzic, R.R. Highly active and durable nanostructured molybdenum carbide electrocatalysts for hydrogen production. *Energy Environ. Sci.* **2013**, *6*, 943–951. [[CrossRef](#)]
49. Liu, D.; Quek, X.Y.; Cheo, W.N.E.; Lau, R.; Borgna, A.; Yang, Y. MCM-41 supported nickel-based bimetallic catalysts with superior stability during carbon dioxide reforming of methane: Effect of strong metal-support interaction. *J. Catal.* **2009**, *266*, 380–390. [[CrossRef](#)]
50. Galetti, A.E.; Gomez, M.F.; Arrúa, L.A.; Abello, M.C. Hydrogen production by ethanol reforming over NiZnAl catalysts: Influence of Ce addition on carbon deposition. *Appl. Catal. A Gen.* **2008**, *348*, 94–102. [[CrossRef](#)]
51. Cárdenas-Arenas, A.; Quindimil, A.; Davó-Quiñonero, A.; Bailón-García, E.; Lozano-Castelló, D.; De-La-Torre, U.; Pereda-Ayo, B.; González-Marcos, J.A.; González-Velasco, J.R.; Bueno-López, A. Isotopic and in situ DRIFTS study of the CO₂ methanation mechanism using Ni/CeO₂ and Ni/Al₂O₃ catalysts. *Appl. Catal. B Environ.* **2020**, *265*, 118538. [[CrossRef](#)]
52. Coenen, K.; Gallucci, F.; Mezari, B.; Hensen, E.; Annaland, M.V.S. An in-situ IR study on the adsorption of CO₂ and H₂O on hydrotalcites. *J. CO₂ Util.* **2018**, *24*, 228–239. [[CrossRef](#)]
53. Quindimil, A.; Onrubia-Calvo, J.A.; Davó-Quiñonero, A.; Bermejo-López, A.; Bailón-García, E.; Pereda-Ayo, B.; Lozano-Castelló, D.; González-Marcos, J.A.; Bueno-López, A.; González-Velasco, J.R. Intrinsic kinetics of CO₂ methanation on low-loaded Ni/Al₂O₃ catalyst: Mechanism, model discrimination and parameter estimation. *J. CO₂ Util.* **2022**, *57*, 101888. [[CrossRef](#)]
54. Proaño, L.; Tello, E.; Arellano-Trevino, M.A.; Wang, S.; Farrauto, R.J.; Cobo, M. In-situ DRIFTS study of two-step CO₂ capture and catalytic methanation over Ru, “Na₂O”/Al₂O₃ Dual Functional Material. *Appl. Surf. Sci.* **2019**, *479*, 25–30. [[CrossRef](#)]
55. Zhou, M.; Andrews, L. Infrared spectra of the CO₂– and C₂O₄– anions isolated in solid argon. *J. Chem. Phys.* **1999**, *110*, 2414–2422. [[CrossRef](#)]
56. Bhattacharyya, K.; Danon, A.; K.Vijayan, B.; Gray, K.A.; Stair, P.C.; Weitz, E. Role of the Surface Lewis Acid and Base Sites in the Adsorption of CO₂ on Titania Nanotubes and Platinized Titania Nanotubes: An in Situ FT-IR Study. *J. Phys. Chem. C* **2013**, *117*, 12661–12678. [[CrossRef](#)]
57. Morales, A.; Agudelo, M.M.R.D.; Hernández, F. Adsorption mechanism of phosphorus on alumina. *Appl. Catal.* **1988**, *41*, 261–271. [[CrossRef](#)]
58. Lewis, J.M.; Kydd, R.A. Adsorption mechanism of phosphoric acid on γ -alumina. *J. Catal.* **1991**, *132*, 465–471. [[CrossRef](#)]
59. Veen, J.A.R.H.V.; Hendriks, P.A.J.M.; Andrea, R.R.; Romers, E.J.G.M.; Wilson, A.E. Chemistry of phosphomolybdate adsorption on alumina surfaces. 2. The molybdate/phosphated alumina and phosphomolybdate/alumina systems. *J. Phys. Chem.* **1990**, *94*, 5282–5285. [[CrossRef](#)]